

Enhancing Fault-Tolerant Surface Code Decoding with Iterative Lattice Reweighting

Yi Tian,^{1,*} Y. Zheng,^{2,*} Xiaoting Wang,^{1,†} and Ching-Yi Lai^{3,‡}

¹*Institute of Fundamental and Frontier Sciences,
University of Electronic Science and Technology of China, Chengdu 610051, China*

²*Furlet Technology, Shanghai 200136, China*

³*Institute of Communications Engineering, National Yang Ming Chiao Tung University, Hsinchu 30010, Taiwan*
(Dated: September 10, 2025)

Efficient and realistic error decoding is crucial for viable fault-tolerant quantum computation (FTQC) on near-term quantum devices. While decoding is a classical post-processing task, its effectiveness relies heavily on accurately modeling quantum noise, which is inherently hardware-dependent. Specifically, correlated bit-flip (X) and phase-flip (Z) errors frequently emerge under realistic circuit-level noise. We introduce the Iterative Reweighting Minimum-Weight Perfect Matching (IRMWPM) decoder, which systematically incorporates such correlations to enhance quantum error correction. Our approach leverages fault-detection patterns to guide the reweighting: we identify correlated X and Z detection events and use their conditional probabilities to update weights on the primal and dual decoding lattices. This iterative procedure improves the decoder's ability to handle realistic error propagation in a hardware-agnostic yet noise-aware manner. We further prove that the IRMWPM decoder converges in finite time while preserving the distance guarantee of the original MWPM algorithm. Under circuit-level noise, our numerical results show substantial improvements in decoding performance. For code distances ≥ 17 and physical error rates ≤ 0.001 , IRMWPM reduces logical error rates by over $20\times$ while maintaining computational efficiency with only a few iterations. It also raises the accuracy threshold from 1% to 1.16%, making it well-suited for near-term, real-time decoding in practical quantum computing architectures. Extrapolated estimates based on our simulation fits suggest that to reach a logical error rate of 10^{-16} , IRMWPM requires only distance $d = 31$, whereas standard MWPM would require $d = 50$, implying a substantial reduction in qubit overhead for achieving high-accuracy FTQC. These results make our method well-suited for near-term, real-time decoding in practical quantum computing architectures.

I. INTRODUCTION

Quantum noise presents a significant challenge to the realization of reliable quantum computation. To overcome this, the development of quantum error-correcting codes (QECCs) and fault-tolerant quantum computation (FTQC) is essential [1–4]. It has been rigorously established that large-scale quantum computation is achievable if the physical noise remains sufficiently local and below a critical threshold [1, 2, 5, 6].

Recent advances in hardware platforms—such as superconducting qubits [7–11], trapped ions [12–14], and neutral atom systems [15–18]—have enabled devices with dozens of qubits and demonstrated the key control and fidelity necessary for proof-of-principle demonstrations of fault-tolerant quantum error correction (FTQEC). Among QECCs, surface codes have emerged as leading candidates due to their local stabilizer structure, high thresholds, and amenability to scalable hardware [19–22].

In FTQEC, syndrome extraction produces a continuous stream of data that must be decoded promptly to identify the locations and types of errors. An effective decoder can achieve code-capacity performance, enabling smaller code distances and reducing overall resource overhead. To

support real-time processing and prevent backlog accumulation, decoding must keep pace with syndrome extraction rates—particularly before executing non-Clifford operations [23–26]. This necessitates a careful balance between decoder complexity and performance, which is critical for scalable FTQC.

A wide range of decoders have been proposed for surface codes, including Minimum Weight Perfect Matching (MWPM) [21, 27–30], Union-Find (UF) [31, 32], renormalization group (RG) [33, 34], belief propagation (BP) [35, 36], Markov chain Monte Carlo (MCMC) [37], tensor networks (TN) [38, 39], and neural networks (NN) [40–46]. Each approach comes with trade-offs in accuracy, complexity, and scalability [47].

For example, RG and BP decoders achieve $O(L^2 \log L)$ complexity for distance- L codes, but both methods lack theoretical guarantees for their decoding performance at low error rates [34, 35]. MCMC methods yield improved thresholds but incur higher computational costs. TN methods are effective under general noise models, but their performance under noisy syndrome extraction remains unclear. NN decoders provide fast inference after training but struggle to generalize across code sizes.

The UF decoder offers linear-time complexity and favorable scalability for near-term deployment [31, 32, 48–50], while MWPM remains the most widely used high-performance decoder. MWPM achieves a threshold near the optimal under circuit-level noise but exhibits high computational complexity, particularly in the presence of measurement errors. Improvements such as Sparse

* These two authors contributed equally to this work.

† xiaoting@uestc.edu.cn

‡ cylai@nycu.edu.tw

Blossom and Parity Blossom reduce its average-case runtime to $O(L^3)$ [28–30], greatly improving its practical utility on devices like Field-Programmable Gate Array (FPGA) [51].

One limitation of the standard MWPM decoder is its independent treatment of X and Z errors, neglecting correlations that arise in noise models such as depolarizing noise. For instance, the presence of a Z error implies a 50% chance of a co-occurring X error on the same qubit, motivating the use of correlated decoding strategies [52, 53]. Note that such X - Z correlations are prevalent in realistic noise channels of quantum memories and gates beyond depolarization noise.

We study an iterative MWPM scheme that reweights the X and Z decoding graphs using the most recent estimates from the dual lattice. This idea is not new: Fowler explicitly described a single reweighting step under the code-capacity noise model [52], which inspired subsequent work on iterative reweighting [54, 55]. However, prior approaches capture only simple correlations and do not analyze the richer X/Z correlations induced by two-qubit CNOT errors—a dominant factor in the circuit-level noise model with noisy syndrome-extraction circuits. Moreover, it remains unclear whether such iterative strategies preserve the decoding radius of standard MWPM. For example, recent work has shown that iterative versions of the UF decoder can violate the distance guarantees of the original UF decoder [56].

In this paper, we propose a fault-tolerant iterative reweighting MWPM (IRMWPM) decoder that systematically exploits X/Z error correlations by leveraging known fault-path structures in noisy syndrome measurements [27]. By identifying correlated detection event patterns and calculating their conditional probabilities (Table III), we develop a principled, data-driven reweighting strategy. Our IRMWPM decoder alternates weight updates between the 3D primal and dual decoding lattices, enhancing its ability to capture realistic error propagation. We prove that IRMWPM converges in finite time, with empirical results showing that only two to four iterations are typically sufficient at practical error rates. Finally, we prove that IRMWPM preserves the decoding radius of the original MWPM decoder.

II. RESULTS

We propose the IRMWPM decoder, which exploits X - Z correlations arising from circuit-level noise. In this section, we illustrate the decoding procedure, present its theoretical guarantees, and demonstrate its performance through numerical simulations. The complete decoding algorithm is given in Algorithm 1.

A. Iterative reweighting decoding strategy

Let $\mathcal{L}_X^{(j)}$ and $\mathcal{L}_Z^{(j)}$ denote the decoding lattices for X -type and Z -type errors, respectively, after j rounds of reweighting for a given error syndrome. Let $\mathcal{M}_X^{(j)}$ and $\mathcal{M}_Z^{(j)}$ be the corresponding outputs of the MWPM algorithm applied to $\mathcal{L}_X^{(j)}$ and $\mathcal{L}_Z^{(j)}$. In particular, $\mathcal{L}_X^{(0)}$ and $\mathcal{L}_Z^{(0)}$ are the initial decoding lattices from given error syndromes S_X and S_Z for the X and Z errors, and $\mathcal{M}_X^{(0)}$ and $\mathcal{M}_Z^{(0)}$ are the initial correction outputs from the standard MWPM decoder.

The iterative decoding process proceeds as follows. First, use $\mathcal{M}_X^{(0)}$ to reweight $\mathcal{L}_Z^{(0)}$ and obtain an updated lattice $\mathcal{L}_Z^{(1)}$. Next, apply the MWPM algorithm to $\mathcal{L}_Z^{(1)}$ to obtain a new matching $\mathcal{M}_Z^{(1)}$. Then, use $\mathcal{M}_Z^{(1)}$ to reweight $\mathcal{L}_X^{(0)}$ and obtain $\mathcal{L}_X^{(1)}$, followed by applying MWPM to get $\mathcal{M}_X^{(1)}$. This sequence constitutes one full iteration. The process is repeated, alternating between reweighting and decoding X -type and Z -type lattices, until the decoding results converge or a predefined iteration limit is reached. Figure 1 illustrates the IRMWPM decoding framework.

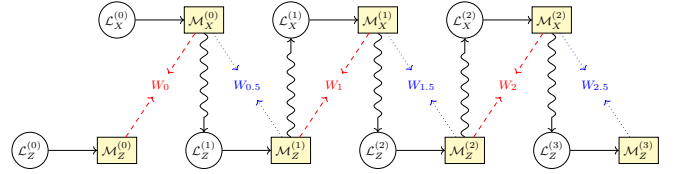


FIG. 1. Illustration of the iterative decoding framework.

1. Reweighting strategy

The IRMWPM decoder differs from the conventional MWPM decoder by dynamically updating edge weights on the decoding lattice based on dual-lattice matching outcomes, whereas MWPM uses fixed weights throughout decoding.

The X and Z decoding lattices are dual to each other. In the iterative reweighting procedure, the edge weights in one lattice are updated based on the decoding outcomes of its dual. To exploit realistic fault correlations in circuit-level noise, we incorporate information about fault-induced correlations between detection events on the X and Z decoding lattices, as identified in Wang et al. [27]. Specifically, we classify and group detection event matchings that arise from single faults, such as CNOT errors, data qubit errors, or measurement faults, as shown in Fig. 2.

Each single fault may produce simultaneous detection events on both the X and Z decoding lattices. For instance, a single Y error on a data qubit can trigger correlated detection events corresponding to matching edges

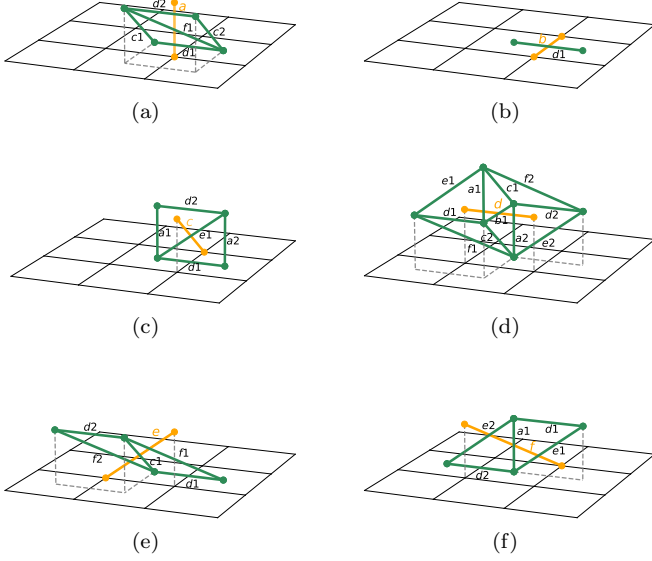


FIG. 2. Decoding lattices \mathcal{L}_X for $L = 3$. When there is an X error matching (orange edge), the corresponding Z error matching (green edge) in \mathcal{L}_Z needs to be reweighted.

in both lattices. These correlated edge patterns are systematically categorized into six types (a–f), each of which appears as a characteristic “thick edge” in the decoding graph. The resulting correlated pairs of detection events are matched across primal and dual lattices, forming fault-path structures that can be used to compute conditional probabilities of dual lattice matchings given observed primal events.

Using this classification, we identify detection event pairs that frequently co-occur due to a common fault source and use their empirical joint and conditional probabilities to reweight edges in the dual decoding lattice. This principled, data-driven approach allows us to iteratively update the edge weights between the primal and dual lattices during decoding, improving the MWPM decoder’s ability to capture realistic error propagation patterns. These conditional probabilities are summarized in Table III (Section IV).

2. Theoretical Guarantees of IRMWPM

Define $\hat{E}^{(j)}$ as the Pauli correction associated with $\mathcal{M}_X^{(j)}$ and $\mathcal{M}_Z^{(j)}$, and let $\hat{E}^{(j+0.5)}$ denote the correction associated with $\mathcal{M}_X^{(j)}$ and $\mathcal{M}_Z^{(j+1)}$. For each integer $j \geq 0$, define $W_j = \text{wt}(\hat{E}^{(j)})$ and $W_{j+0.5} = \text{wt}(\hat{E}^{(j+0.5)})$ as the total weights of the corresponding corrections. These quantities are also illustrated in Fig. 1.

We prove in Lemma 3 (Section IV) that the sequence W_j is nonincreasing and stabilizes in finite time. This leads to the following result:

Theorem 1. The IRMWPM decoder converges in finite time.

In practice, our simulations show rapid convergence, typically within 2–4 iterations for realistic error rates in the range of 10^{-3} to 10^{-4} .

We prove that the IRMWPM decoder achieves the same decoding radius as the standard MWPM decoder, thereby preserving its distance guarantee.

Theorem 2. [IRMWPM] Let E be an n -qubit Pauli error with weight at most $\lfloor \frac{d-1}{2} \rfloor$. If E is correctable by the MWPM decoder on a surface code of distance d under either the code capacity or circuit-level noise model, then E is also correctable by the IRMWPM decoder, assuming that the final round of syndrome measurements is perfect.

B. Numerical Simulations

We numerically evaluate the performance of the proposed IRMWPM decoder under the standard symmetric circuit-level depolarizing noise model, focusing on its impact on logical error rates, threshold behavior, and decoding efficiency.

The simulation proceeds as follows: For a distance- L surface code, we assume noisy syndrome extraction (SE) with circuit-level noise in each round. After performing L rounds of SE, a decoder is applied using the accumulated syndromes. In addition, every T SE cycles, a virtual decoding step is performed using an ideal decoder that assumes one round of perfect measurements and operates on a 2D lattice to check for logical errors. If no logical error is detected, noisy SE continues. This process repeats until a logical error occurs, and we record the total number of SEs. We repeat this procedure to compute the average logical qubit lifetime. In the following simulations, we set $T = L$. Similar lifetime simulations were conducted in [36] using BP decoding. We show that IRMWPM achieves better performance.

In a single run of IRMWPM, iterations stop once the decoding result repeats (i.e., the same result is obtained in two consecutive iterations), which typically occurs within 2–4 iterations in our simulations. Correction weight stabilization can also serve as a secondary stopping criterion if perfect convergence is desired.

Benchmark simulations are conducted using surface codes of distance $L = 5, 7, 9, 13, 17$, with a decoding period of $T = L$ rounds of syndrome extraction.

The decoding threshold denotes the physical error rate below which the logical error rate can be suppressed arbitrarily by increasing the surface code distance. As shown in Fig. 3, the standard MWPM decoder yields a threshold of approximately 1%, while the IRMWPM decoder achieves a higher threshold of about 1.16%, representing a 16% improvement.

Next, we examine the impact of iterative lattice reweighting on the decoding error rate of MWPM decoders, particularly in the low physical error rate regime.

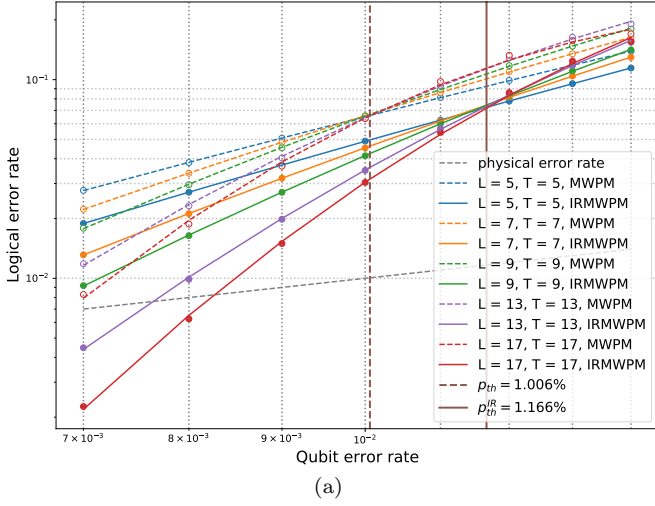


FIG. 3. Comparison of decoding thresholds achieved by the MWPM and IRMWPM decoders.

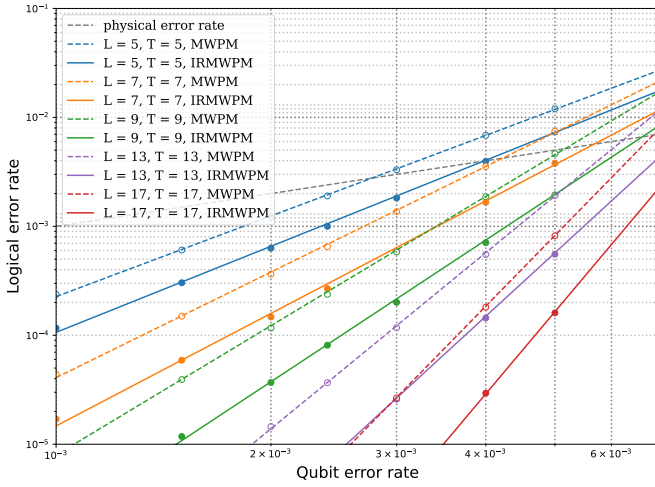


FIG. 4. Decoding performance of MWPM and IRMWPM decoders at low physical error rates.

As illustrated in Fig. 4, iterative reweighting significantly reduces the decoding error rate. For example, at a physical error rate of $p = 0.24\%$ and a surface code distance of $L = 13$, the IRMWPM decoder achieves an approximately 80% reduction in decoding error rate compared to the standard MWPM decoder.

Here, we quantitatively evaluate the improvement in the performance of the MWPM decoder using iterative lattice reweighting across physical error rates p and surface code distances L . As shown in Fig. 5, the advantage of this iterative approach becomes more significant at lower p and larger L , leading to a more substantial reduction in decoding error rates. To estimate the logical error rates for both MWPM and IRMWPM decoders, we extrapolate from the data in Fig. 4, which is fitted using the following general equation:

$$P_L(p, L) = 10^{aL^2 + bL + c} p^{eL^2 + fL + g}, \quad (1)$$

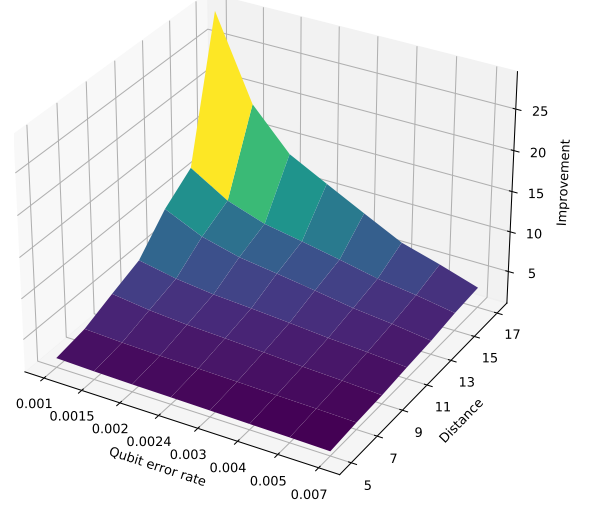


FIG. 5. Impact of iterative lattice reweighting on decoding performance across different physical error rates and surface code distances.

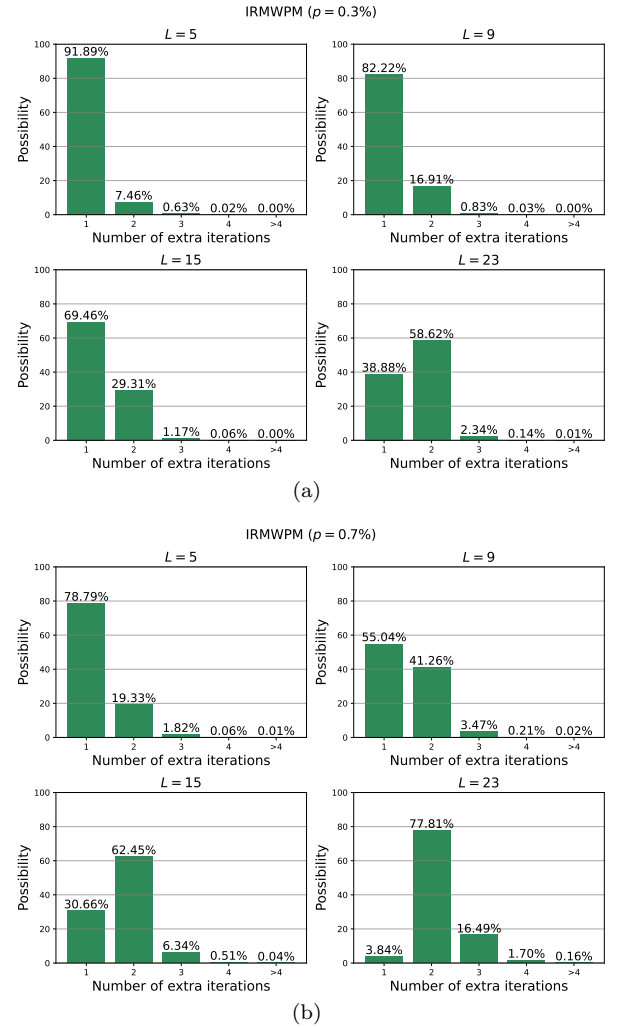


FIG. 6. Number of additional iterations required for convergence under various physical error rates and surface code distances in the IRMWPM decoder.

where a, b, c, e, f , and g are fitted parameters. Extrapolating to $L = 31$ and $p = 0.001$ (a typical regime for large-scale FTQC running Shor's algorithm), we find $P_L \approx 3 \times 10^{-12}$ for MWPM and 3×10^{-16} for IRMWPM, respectively, showing a reduction of approximately four orders of magnitude. To match the same logical error rate using standard MWPM, a surface code of distance $L \geq 50$ is needed. Thus, IRMWPM offers a physical qubit saving of over 60% per logical qubit.

While iterative reweighting enhances decoding performance, it introduces additional computational cost due to multiple iterations. Assessing convergence requirements is thus critical: as shown in Fig. 6, the IRMWPM decoder averages only a few extra iterations,

For $L = 23$, four iterations are sufficient for 99%+ of cases at $p = 0.3\%$. When operating at the lower physical error rates, this average would be significantly less, keeping the overall computational complexity comparable to standard MWPM.

III. DISCUSSION

This work presents the IRMWPM decoder as a principled and scalable enhancement MWPM decoding under circuit-level noise. By systematically incorporating known fault-path correlations into an iterative lattice reweighting process, IRMWPM improves decoding accuracy while preserving the distance guarantee of the original decoder. In contrast to previous reweighting strategies, which either lack theoretical justification or are limited to code capacity models, our approach is grounded in well-characterized detection event patterns and fault mechanisms, enabling interpretable and data-driven reweighting on the 3D decoding lattice. We alternately update weights between the primal and dual grids, allowing the decoder to capture realistic error propagation better.

Numerical simulations demonstrate a 16% increase in accuracy threshold and up to an 80% reduction in logical error rate at low physical error rates, all while requiring only a few additional iterations. This efficiency makes IRMWPM particularly suitable for near-term, real-time deployment in fault-tolerant quantum architectures.

IRMWPM converges quickly in practice, as shown by our simulations. We formally prove its finite-time convergence by demonstrating that the total weight of the X and Z error estimates constitutes a non-increasing sequence of non-negative integers. This not only guarantees convergence but also yields a straightforward, weight-based termination criterion. This leads to an open theoretical challenge: proving IRMWPM's convergence within $O(\text{poly}(\log L))$.

These results highlight the practical value of leveraging correlated errors in decoding, without sacrificing theoretical robustness. Future directions include extending this framework to other topological codes, exploring approximate fault models for broader applicability. Given the significant progress in deploying MWPM on FPGAs

to achieve microsecond-level decoding latency for code length $L = 13$ [51], IRMWPM, which incurs lower overhead than MWPM, holds promise for high-performance real-time quantum error correction when implemented on FPGAs or ASICs.

The software developed in this paper is available at Github [57].

IV. METHOD

A. Preliminaries

1. Pauli operators

We consider errors that are tensor products of Pauli operators I, X, Y, Z . A single-qubit Pauli operator can be expressed as $X^a Z^b$ for $a, b \in \{0, 1\}$, up to a global phase, where $X^0 = I = Z^0$, $X^1 = X$, and $Z^1 = Z$. In general, an n -fold Pauli operator can be expressed as $X^{\mathbf{a}} Z^{\mathbf{b}} \triangleq \bigotimes_{j=1}^n X^{a_j} Z^{b_j}$, where $\mathbf{a} = a_1 \cdots a_n$ and $\mathbf{b} = b_1 \cdots b_n$, up to a global phase. For simplicity, a Pauli operator E is written as $E = E_X E_Z$, where E_X and E_Z denote its X and Z components, respectively.

The support of a Pauli error E is the set of qubits where E acts nontrivially. Let $\text{wt}(E)$ denote the weight of a Pauli operator E , defined as the number of its nontrivial components, which is the size of its support. Additionally, we use $\text{wt}(\mathbf{a})$ to denote the Hamming weight of the binary vector \mathbf{a} .

2. Surface code

The surface code is a quantum error-correcting code implemented on a two-dimensional lattice of physical qubits. We focus on the $[[L^2 + (L - 1)^2, 1, L]]$ surface code [20], which encodes a single logical qubit into $L^2 + (L - 1)^2$ physical qubits arranged on a lattice of length L , as illustrated in Fig. 7 for the case of $L = 3$.

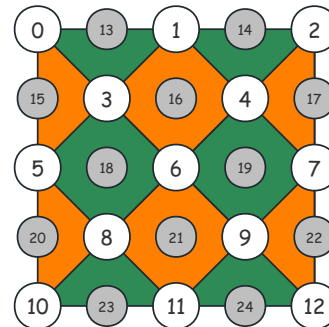


FIG. 7. Implementation of a distance-3 surface code on a two-dimensional lattice, where gray circles denote measurement qubits and white circles represent data qubits.

In this layout, physical qubits are categorized into two

types: measurement qubits, shown as gray circles in Fig. 7, and data qubits, represented by white circles. Each data qubit participates in at least two stabilizer generators, indicated by the orange and green color blocks. Each block corresponds to a measurement qubit and its adjacent data qubits, forming a Pauli stabilizer of weight 3 or 4.

The parameter L also defines the minimum distance of the surface code, which is the minimum weight of a Pauli error that can cause a logical failure. For example, a horizontal X string acting on qubits 10, 11, and 12 constitutes a logical X error.

An X stabilizer is defined by the tensor product of X operators acting on the neighboring data qubits of a measurement qubit in an orange block, with Z stabilizers defined similarly. Measuring these stabilizers determines the parity of the corresponding data qubits in the Z or X basis, as shown in Fig. 8. The measurement outcomes, known as *error syndromes*, help identify both the type and location of errors on the data qubits. Each stabilizer measurement involves initializing a measurement qubit, applying four CNOT gates with adjacent data qubits, and performing a final measurement. This process is also referred to as *syndrome extraction* (SE).

For more efficient practical simulations, we adopt a reduced-depth implementation of the SE circuit consisting of five steps, by removing the I and H gates and instead preparing ancilla qubits in the $|0\rangle$ and $|+\rangle$ states, with measurements performed in the Z and X bases.

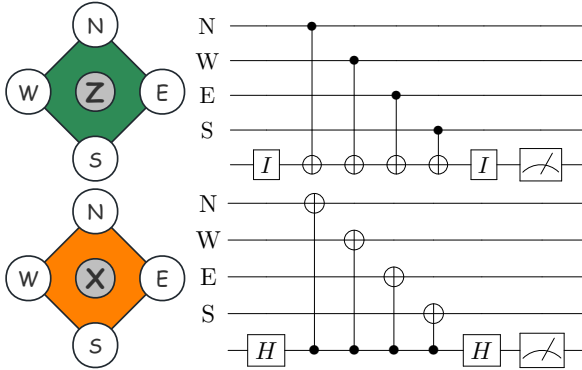


FIG. 8. Standard Z - and X -stabilizer syndrome extraction circuits for the surface code. N, W, E, and S denote the data qubits located to the north, west, east, and south of the measurement qubits, respectively. Weight-three stabilizers can be measured in a similar manner.

3. Noise model

We define the terminology and noise model as follows.

A fault refers to a malfunction or imperfection in a physical operation or process, while an error is the unintended deviation in the quantum state resulting from such a fault. For example, a single-qubit gate fault may introduce a Pauli error on the affected qubit.

In this work, we adopt a standard circuit-level depolarizing noise model for gate and measurement faults in SE, where p denotes the fault rate [27]. Our syndrome extraction circuits include the following three types of faults:

- (1) Following the execution of a single-qubit identity I or the Hadamard gate H , a Pauli error from $\{X, Y, Z\}$ is applied to the data qubit with probability $p/3$.
- (2) After each two-qubit CNOT gate, a two-qubit Pauli error is uniformly and randomly drawn from the set $\{I, X, Y, Z\}^{\otimes 2} \setminus \{I \otimes I\}$ with probability $p/15$.
- (3) Performing a two-outcome measurement produces an incorrect outcome with probability p .

A round of SE for all X -type and Z -type stabilizers can be performed in parallel using the circuits shown in Fig. 8. However, due to imperfections in the involved gates and measurements, error syndromes may be incorrect. Decoding based on such faulty syndromes can lead to a high probability of logical errors. For a surface code of distance L , it generally requires decoding over T rounds of SE to ensure fault tolerance, where $T = O(L)$ [21]. In this paper, we set $T = L$.

4. Decoding lattice and the MWPM decoder

In the circuit-level noise model, the decoding lattice for surface codes is a 3D space-time graph that accounts for possible faults across multiple rounds of syndrome extraction [27, 58]. Two separate decoding lattices are used for decoding X -type and Z -type errors, respectively. Each stabilizer measurement at different time steps is represented by a check node. Within a single round, two check nodes are connected if they involve the same qubits. For example, measurement errors induce vertical edges connecting the same stabilizer across two consecutive rounds. Additionally, CNOT-induced faults create characteristic edge patterns between check nodes across time steps, capturing the correlated nature of propagated errors. Figure 9 illustrates the decoding lattice for Z -type stabilizers with $L = 3$.

A *detection event* occurs when the measured syndrome of a stabilizer differs from that in the previous round, indicating a nontrivial syndrome at the corresponding check node. By analyzing detection events between connected check nodes, each connecting edge is assigned a weight proportional to $-\ln P$, where the error probability P (as a function of the physical error rate p) captures the cumulative effect of noisy stabilizer measurements and error propagation [27, 58]. In general, using a more accurate decoding lattice, which may incorporate additional circuit-level information, can improve decoding performance [27, 52].

X -type and Z -type errors are handled separately by the MWPM decoder. Given a 3D space-time decoding

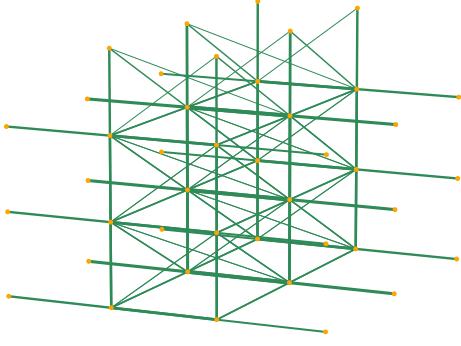


FIG. 9. Standard circuit-level depolarization noise decoding lattice for Z -stabilizers with distance 3. The edge thickness in the lattice is proportional to $-\ln P$, where P is the overall probability of faults contributing to that edge.

lattice and the measured syndromes for either X -type or Z -type errors, a standard MWPM decoder identifies the minimum weight perfect matching in the lattice. This matching corresponds to the most likely error pattern that explains the observed syndromes by connecting them in the decoding lattice.

B. IRMWPM

It has been shown that iteratively applying MWPM decoding for X - and Z -type errors with reweighting substantially improves decoding performance [52–55]. In this section, we describe the IRMWPM decoder with reweighting strategies. The following subsections detail the reweighting strategies employed in our iterative decoder.

1. Code capacity noise model

We start with the simpler code capacity noise model, where syndrome extraction circuits are perfect and the decoding lattice constitutes a single horizontal layer, and then extend the analysis to the circuit-level noise model.

A single-qubit Pauli error can be expressed as $X^a Z^b$ for $a, b \in \{0, 1\}$, up to a global phase. The joint probability distribution of X^a and Z^b under the depolarizing noise model is given in Table I. In this representation, the two types of errors are not independent. In fact, the conditional probabilities $\Pr(X|Z) = \Pr(Z|X) = 1/2$ indicate that the occurrence of one type of error significantly increases the likelihood of the other, raising it from $p/3$ to $1/2$. However, standard MWPM decoding neglects the correlations between X - and Z -type errors, making it suboptimal.

By incorporating these correlations, the weights of the Z -error decoding lattice can be updated based on the decoding results for X errors, and vice versa. This iterative process continues for both X and Z errors until the

Algorithm 1: Iterative Minimum Weight Perfect Matching (IRMWPM) Decoder

Input: X syndrome S_X , Z syndrome S_Z , maximum iterations T_{\max}
Output: X error estimate \hat{E}_X , Z error estimate \hat{E}_Z
// Initialization
 $\hat{E}_X^{(0)} \leftarrow \emptyset$;
 $\hat{E}_Z^{(0)} \leftarrow \emptyset$;
 $k \leftarrow 0$ **// Iteration counter**
Construct X decoding graph \mathcal{L}_X from syndrome S_X
Construct Z decoding graph \mathcal{L}_Z from syndrome S_Z
while $k < T_{\max}$ **do**
 // X Decoding Step
 Reweight($\mathcal{L}_X, \hat{E}_Z^{(k)}$);
 $\hat{E}_X^{(k+1)} \leftarrow \text{MWPM}(\mathcal{L}_X)$;
 // Z Decoding Step
 Reweight($\mathcal{L}_Z, \hat{E}_X^{(k+1)}$);
 $\hat{E}_Z^{(k+1)} \leftarrow \text{MWPM}(\mathcal{L}_Z)$;
 // Stopping Criteria
 if $\exists j, l \leq k, \hat{E}_X^{(k+1)} = \hat{E}_X^{(j)} \parallel \hat{E}_Z^{(k+1)} = \hat{E}_Z^{(l)}$, **then**
 break **// Error estimates converged**
 $k \leftarrow k + 1$;
end
return $\hat{E}_X^{(k+1)}, \hat{E}_Z^{(k+1)}$

$a \backslash b$	0	1
	0	1
0	$1 - p$	$p/3$
1	$p/3$	$p/3$

TABLE I. Joint probability distribution of X^a and Z^b for single-qubit gates.

decoding results converge or a predefined iteration limit is reached. More precisely, the weight of an edge is determined by the associated conditional probability. When the conditional probability $\Pr(X|Z) = \Pr(Z|X) = 1/2$ is considered, the edge weight is effectively reduced, making it a more favorable matching option.

For simplicity, the weight of an unconditioned edge is normalized to 1, whereas an edge conditioned on the presence of an error in the dual lattice is reweighted to 0.

Figure 10 provides a simple example illustrating the decoding process of this strategy in a 2D grid when SE is noiseless. First, the syndromes for X - and Z -type errors are extracted (Fig. 10(a)) and decoded separately to obtain their respective initial decoding results (Fig. 10(b)). The decoding results for Z errors are then used to update the decoding lattice for X errors, leading to refined decoding results for X errors (Fig. 10(c)). Next, these updated X -error decoding results are used to adjust the decoding lattice for Z errors, yielding improved decoding results for Z errors (Fig. 10(d)).

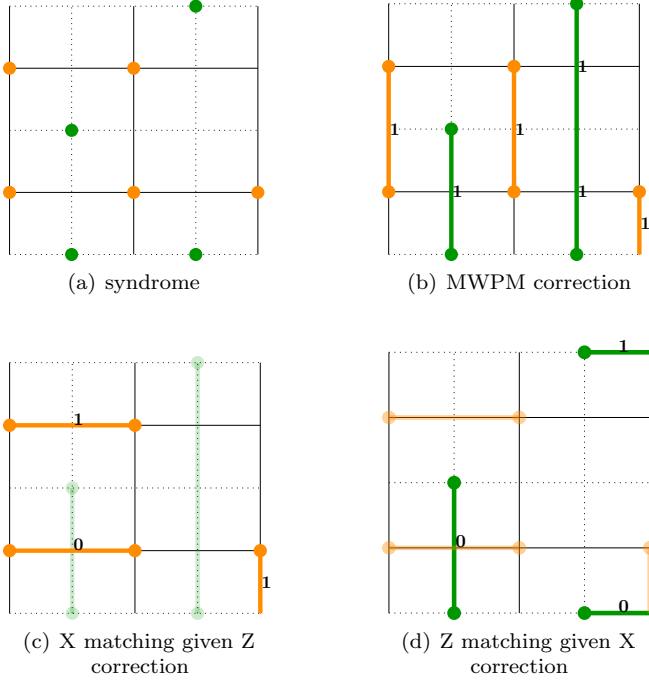


FIG. 10. An example of the iterative weighted strategy on 2D decoding lattices, where green and orange dots represent nontrivial syndromes, and colored edges indicate perfect matchings.

2. Circuit-level noise model

Next, we extend this iterative reweighting decoding procedure to the circuit-level noise model in FTQC, accounting for noise correlations from error propagation through noisy CNOT gates, which has been studied in [52, 59]. To support reweighting, we propose a systematic method for constructing the conditional probabilities of these correlated events.

Decoding circuit-level noise introduces additional complexities. In the case of noiseless SEs, each edge in the decoding lattice corresponds to a single location fault, making error identification straightforward. However, for circuit-level noise in 3D decoding lattices, a single edge often results from multiple faults across different gates and qubits.

A two-qubit Pauli error generated from two-qubit CNOT gates can be represented as $X^{a_1 a_2} Z^{b_1 b_2}$ for $a_1, a_2, b_1, b_2 \in \{0, 1\}$, up to a global phase. The joint probability distribution of $X^{a_1 a_2}$ and $Z^{b_1 b_2}$ errors for two-qubit gate faults is given in Table II. Handling X - and Z -type errors separately can be achieved by considering the distributions of $a_1 a_2$ and $b_1 b_2$ independently. For

instance,

$$\Pr(X^{a_1 a_2}) = \sum_{b'_1, b'_2=0}^1 \Pr(X^{a_1 a_2} Z^{b'_1 b'_2}) = \frac{4p}{15},$$

$$\Pr(Z^{b_1 b_2}) = \sum_{a'_1, a'_2=0}^1 \Pr(X^{a'_1 a'_2} Z^{b_1 b_2}) = \frac{4p}{15}$$

for $a_1 a_2 \neq 00$ and $b_1 b_2 \neq 00$.

$a_1 a_2 \backslash b_1 b_2$	00	01	10	11
00	$1 - p$	$p/15$	$p/15$	$p/15$
01	$p/15$	$p/15$	$p/15$	$p/15$
10	$p/15$	$p/15$	$p/15$	$p/15$
11	$p/15$	$p/15$	$p/15$	$p/15$

TABLE II. Joint probability distribution of $X^{a_1 a_2}$ and $Z^{b_1 b_2}$ errors for CNOT gates.

In [27], single fault mechanisms on surface code decoding lattices, arising from CNOT faults, data qubit faults, and measurement faults, are carefully classified, identifying 23 basic error matchings for each X or Z decoding lattice. Each error matching is represented by a thick edge connecting two detection events and is categorized into one of six types on the X decoding lattice. These six types, labeled a through f, are illustrated as orange strings in Fig. 2. For example, the error matching a in Fig. 2 (a) represents a temporal edge connecting two check nodes corresponding to the same stabilizer across consecutive layers, which may arise from a measurement fault or a CNOT fault that leaves a residual Pauli error on the measurement qubit.

Also shown in Fig. 2, each type of orange error matching has corresponding green error matches on the dual lattice that may occur simultaneously due to the same fault source. For instance, in Fig. 2 (c), the matchings a_1 and a_2 correspond to the same type as matching a in Fig. 2 (a). Every green matching in the dual lattice is correlated with the orange matching in the same subfigure. For example, the matchings b and d_1 in Fig. 2 (b) both originate from a single Y error on the data qubit located at the intersection of the two matchings. These six groups of subfigures in Fig. 2 are adapted from the classifications in [27] by pairing matchings that arise from the same fault source. For example, in the X -stabilizer SE in Fig. 8, a two-qubit error $X^{01} Z^{10}$ on the control and target qubits after the first CNOT gate results in matchings a and d_1 in Fig. 2 (a). A similar correlation structure applies to the Z decoding lattice.

In the preceding discussion, each type of error matching in a decoding lattice is associated with a specific occurrence probability. We now examine how the presence of a particular error matching on one decoding lattice may influence its counterpart on the dual lattice. This reweighting process is guided by conditional probabilities between such correlated edges, effectively transforming

a static decoding graph into a dynamic graph that captures the fault correlations imposed by the physical noise model.

To simplify the calculation, we adopt a direct summation approach to estimate the occurrence probability of each type of error matching, under the assumption of a low physical error rate p . For instance, the orange error matching a in Fig. 2 (a) can result from four distinct CNOT gate faults and one measurement fault, corresponding to five out of the 23 error matchings identified in [27]. The approximate occurrence probability is given by

$$P(a) = 4 \cdot \frac{4p}{15} + p = \frac{31p}{15}. \quad (2)$$

The probabilities for the remaining types of matchings can be computed similarly.

From Fig. 2, it is evident that matchings on a decoding lattice and its dual can be correlated, and the probability of one matching occurring, conditioned on a correlated matching in the dual lattice, can be computed. Consider again the orange error matching a in Fig. 2(a) along with the green error matching d_1 . According to [27, Fig. 3(a) and 3(b)], these syndromes may arise from errors $X^{10}Z^{10}$ or $X^{01}Z^{10}$ (error matchings 1 and 4), or $X^{11}Z^{01}$ (error matchings 7 and 10). Thus, the joint probability of occurrence is $P(a, d_1) = 3p/15$. From Eq. (2), the conditional probability is $P(d_1|a) = P(a, d_1)/P(a) = 3/31$, which is significantly higher than the standalone probability of d_1 , given by $P(d_1) = 42p/15$. Therefore, we reassign the weight of d_1 in the dual lattice as $-\ln(P(d_1|a))$.

Table III lists the conditional probabilities used to reweight edges that are not near the boundaries of the decoding lattices. For error matchings near the boundary, the corresponding reweighted values may differ due to the reduced number of contributing fault mechanisms.

$P(c_1 a) = \frac{1}{31}$	$P(d_1 c) = \frac{3}{16}$	$P(d_1 d) = \frac{1}{21}$	$P(d_2 e) = \frac{1}{8}$
$P(c_2 a) = \frac{1}{31}$	$P(d_2 c) = \frac{3}{16}$	$P(d_2 d) = \frac{1}{21}$	$P(f_1 e) = \frac{1}{8}$
$P(d_1 a) = \frac{3}{31}$	$P(e_1 c) = \frac{1}{8}$	$P(e_1 d) = \frac{1}{42}$	$P(f_2 e) = \frac{1}{8}$
$P(d_2 a) = \frac{3}{31}$	$P(a_0 d) = \frac{1}{14}$	$P(e_2 d) = \frac{1}{42}$	$P(a_0 f) = \frac{1}{4}$
$P(f_1 a) = \frac{2}{31}$	$P(a_1 d) = \frac{1}{14}$	$P(f_1 d) = \frac{1}{42}$	$P(d_1 f) = \frac{1}{8}$
$P(d_1 b) = \frac{1}{2}$	$P(b_0 d) = \frac{3}{14}$	$P(f_2 d) = \frac{1}{42}$	$P(d_2 f) = \frac{1}{8}$
$P(a_0 c) = \frac{1}{16}$	$P(c_1 d) = \frac{1}{14}$	$P(c_1 e) = \frac{1}{4}$	$P(e_1 f) = \frac{1}{8}$
$P(a_1 c) = \frac{1}{16}$	$P(c_2 d) = \frac{1}{14}$	$P(d_1 e) = \frac{1}{8}$	$P(e_2 f) = \frac{1}{8}$

TABLE III. Conditional probabilities used to reweight correlated error matchings across dual decoding lattices.

Note that this correlation between the two types of errors is quite general and not limited to depolarizing circuit-level noise in practice. For example, non-probabilistic noise channels such as amplitude damping (T_1 process) also exhibit this correlation from a quantum error correction perspective. In this paper, we focus on circuit-level

noise for simplicity. Incorporating these correlations into decoding can also be extended to more realistic noise models in practical scenarios.

3. Theoretical guarantees of IRMWPM

Yuan et al. [54] showed that under the code-capacity noise model, the weight of Pauli correction does not increase across IRMWPM iterations. We extend this result to the circuit-level noise model, enabling a proof of convergence for IRMWPM.

Lemma 3. In IRMWPM decoding under the circuit-level noise model, the weight of the joint Pauli correction is nonincreasing across iterations. Specifically, let $\hat{E}^{(j)}$ denote the joint Pauli X and Z correction obtained after the j -th iteration. Then, for $j \geq 0$,

$$\text{wt}(\hat{E}^{(j)}) \geq \text{wt}(\hat{E}^{(j+0.5)}) \geq \text{wt}(\hat{E}^{(j+1)}).$$

Proof. Let $\text{wt}(\mathcal{L}_X^{(j)}, \mathcal{M}_X^{(k)})$ denote the weight of the matching $\mathcal{M}_X^{(k)}$ on the lattice $\mathcal{L}_X^{(j)}$. These quantities can be expressed as:

$$W_j = \text{wt}(\mathcal{L}_Z^{(0)}, \mathcal{M}_Z^{(j)}) + \text{wt}(\mathcal{L}_X^{(j+1)}, \mathcal{M}_X^{(j)}) \quad (3)$$

$$= \text{wt}(\mathcal{L}_X^{(0)}, \mathcal{M}_X^{(j)}) + \text{wt}(\mathcal{L}_Z^{(j)}, \mathcal{M}_Z^{(j)}) \quad (4)$$

$$W_{j+0.5} = \text{wt}(\mathcal{L}_Z^{(0)}, \mathcal{M}_Z^{(j+1)}) + \text{wt}(\mathcal{L}_X^{(j+1)}, \mathcal{M}_X^{(j)}) \quad (5)$$

$$= \text{wt}(\mathcal{L}_X^{(0)}, \mathcal{M}_X^{(j)}) + \text{wt}(\mathcal{L}_Z^{(j+1)}, \mathcal{M}_Z^{(j+1)}). \quad (6)$$

Equations (3) and (5) compute the total weight by first evaluating the Pauli Z component, followed by the reweighted Pauli X component. Conversely, Equations (4) and (6) begin with the Pauli X part and then account for the corresponding Z part after reweighting.

We now derive the following sequence of inequalities:

$$\begin{aligned} W_0 &= \text{wt}(\mathcal{L}_X^{(0)}, \mathcal{M}_X^{(0)}) + \text{wt}(\mathcal{L}_Z^{(1)}, \mathcal{M}_Z^{(0)}) \\ &\stackrel{(a)}{\geq} \text{wt}(\mathcal{L}_X^{(0)}, \mathcal{M}_X^{(0)}) + \text{wt}(\mathcal{L}_Z^{(1)}, \mathcal{M}_Z^{(1)}) = W_{0.5} \\ &\stackrel{(b)}{=} \text{wt}(\mathcal{L}_Z^{(0)}, \mathcal{M}_Z^{(1)}) + \text{wt}(\mathcal{L}_X^{(1)}, \mathcal{M}_X^{(0)}) \\ &\stackrel{(c)}{\geq} \text{wt}(\mathcal{L}_Z^{(0)}, \mathcal{M}_Z^{(1)}) + \text{wt}(\mathcal{L}_X^{(1)}, \mathcal{M}_X^{(1)}) = W_1, \end{aligned}$$

where inequality (a) follows from the fact that $\mathcal{M}_Z^{(1)}$ is a matching of minimum weight on $\mathcal{L}_Z^{(1)}$, so $\text{wt}(\mathcal{L}_Z^{(1)}, \mathcal{M}_Z^{(0)}) \geq \text{wt}(\mathcal{L}_Z^{(1)}, \mathcal{M}_Z^{(1)})$; equality (b) is due to Eq. (5), which relates the lattices after reweighting; inequality (c) holds because $\mathcal{M}_X^{(1)}$ is a minimum-weight matching on $\mathcal{L}_X^{(1)}$.

By repeating this argument across further iterations, we obtain the monotonic sequence:

$$W_0 \geq W_{0.5} \geq W_1 \geq W_{1.5} \geq \dots,$$

which establishes the claim. \square

We have shown that the sequence $\text{wt}(\hat{E}^{(j)})$ is nonincreasing and bounded below by zero. Therefore, it must stabilize in finite time, establishing the convergence of IRMWPM.

Now we establish the distance guarantee of the IRMWPM decoder. The standard MWPM decoder provides the following distance guarantee.

Lemma 4. [MWPM decoder] Let $E = E_X E_Z$ be an n -qubit Pauli error on a surface code of distance d . If $\text{wt}(E_X) \leq \lfloor \frac{d-1}{2} \rfloor$ and $\text{wt}(E_Z) \leq \lfloor \frac{d-1}{2} \rfloor$, then E is correctable by the MWPM decoder assuming perfect syndrome measurements.

This property is expected to extend to circuit-level noise when more than d rounds of noisy syndrome measurements are used with one additional round of perfect syndrome measurements, although no formal proof currently exists.

The UF decoder offers a similar distance guarantee [31]; however, it has been shown that an iterative UF decoder does not maintain this guarantee on surface codes [56]. This highlights the importance of verifying whether the IRMWPM decoder preserves the same distance guarantee, which we establish in the following.

Theorem 5. [Decoding Radius of IRMWPM] Let E be an n -qubit Pauli error with $\text{wt}(E) \leq \lfloor \frac{d-1}{2} \rfloor$. If E

is correctable by the MWPM decoder, then it is also correctable by the IRMWPM decoder on a surface code of distance d , assuming that the final round of syndrome measurements is perfect.

Proof. Suppose that E has weight $\text{wt}(E) \leq \lfloor (d-1)/2 \rfloor$ and is within the guaranteed decoding radius of MWPM. By the optimality property of MWPM, the initial estimate \hat{E} satisfies: $\text{wt}(\hat{E}) \leq \text{wt}(E) \leq \lfloor \frac{d-1}{2} \rfloor$. By the nonincreasing weight property of IRMWPM in Lemma 3, after one iteration we have estimate \hat{E}' satisfying: $\text{wt}(\hat{E}') \leq \text{wt}(\hat{E}) \leq \lfloor \frac{d-1}{2} \rfloor$.

Since both \hat{E} and \hat{E}' match the syndrome of E , the product $\hat{E}\hat{E}'$ has trivial syndrome. Moreover, $\text{wt}(\hat{E}\hat{E}') \leq \text{wt}(\hat{E}) + \text{wt}(\hat{E}') \leq 2 \lfloor \frac{d-1}{2} \rfloor < d$. By the definition of the code distance d , $\hat{E}\hat{E}'$ is a stabilizer. Hence, \hat{E} and \hat{E}' differ by a stabilizer and yield the same logical correction.

It follows that the IRMWPM decoder produces the same logical outcome as the MWPM decoder when $\text{wt}(E) \leq \lfloor \frac{d-1}{2} \rfloor$. \square

ACKNOWLEDGEMENT

YT and XW were supported by the National Natural Science Foundation of China (Grant No. 92265208). CYL was supported by the National Science and Technology Council in Taiwan, under Grants No. 113-2221-E-A49-114-MY3, No. 113-2119-M-A49-008-, and No. 114-2119-M-A49-006-.

-
- [1] D. Aharonov and M. Ben-Or, Fault-tolerant quantum computation with constant error, in *Proceedings of the twenty-ninth annual ACM symposium on Theory of computing* (1997) pp. 176–188.
 - [2] D. Gottesman, *Stabilizer codes and quantum error correction* (California Institute of Technology, 1997).
 - [3] M. A. Nielsen and I. L. Chuang, *Quantum computation and quantum information* (Cambridge university press, 2010).
 - [4] D. A. Lidar and T. A. Brun, *Quantum error correction* (Cambridge university press, 2013).
 - [5] P. Aliferis, D. Gottesman, and J. Preskill, Quantum accuracy threshold for concatenated distance-3 codes, arXiv preprint quant-ph/0504218 (2005).
 - [6] E. T. Campbell, B. M. Terhal, and C. Vuillot, Roads towards fault-tolerant universal quantum computation, *Nature* **549**, 172 (2017).
 - [7] S. Krinner, N. Lacroix, A. Remm, A. Di Paolo, E. Genois, C. Leroux, C. Hellings, S. Lazar, F. Swiadek, J. Herrmann, *et al.*, Realizing repeated quantum error correction in a distance-three surface code, *Nature* **605**, 669 (2022).
 - [8] Y. Zhao, Y. Ye, H.-L. Huang, Y. Zhang, D. Wu, H. Guan, Q. Zhu, Z. Wei, T. He, S. Cao, *et al.*, Realization of an error-correcting surface code with superconducting qubits, *Phys. Rev. Lett.* **129**, 030501 (2022).
 - [9] R. Acharya, I. Aleiner, R. Allen, T. I. Andersen, M. Ansmann, F. Arute, K. Arya, A. Asfaw, J. Atalaya, R. Babush, D. Bacon, J. C. Bardin, J. Basso, A. Bengtsson, S. Boixo, G. Bortoli, A. Bourassa, J. Bovaird, L. Brill, M. Broughton, B. B. Buckley, D. A. Buell, T. Burger, B. Burkett, N. Bushnell, Y. Chen, Z. Chen, B. Chiaro, J. Cogan, R. Collins, P. Conner, W. Courtney, A. L. Crook, B. Curtin, D. M. Debroy, A. Del Toro Barba, S. Demura, A. Dunsworth, D. Eppens, C. Erickson, L. Faoro, E. Farhi, R. Fatemi, L. Flores Burgos, E. Forati, A. G. Fowler, B. Foxen, W. Giang, C. Gidney, D. Gilboa, M. Giustina, A. Grajales Dau, J. A. Gross, S. Habegger, M. C. Hamilton, M. P. Harrigan, S. D. Harrington, O. Higgott, J. Hilton, M. Hoffmann, S. Hong, T. Huang, A. Huff, W. J. Huggins, L. B. Ioffe, S. V. Isakov, J. Iveland, E. Jeffrey, Z. Jiang, C. Jones, P. Juhas, D. Kafri, K. Kechedzhi, J. Kelly, T. Khat-tar, M. Khezri, M. Kieferová, S. Kim, A. Kitaev, P. V.

- Klimov, A. R. Klots, A. N. Korotkov, F. Kostritsa, J. M. Kreikebaum, D. Landhuis, P. Laptev, K.-M. Lau, L. Laws, J. Lee, K. Lee, B. J. Lester, A. Lill, W. Liu, A. Locharla, E. Lucero, F. D. Malone, J. Marshall, O. Martin, J. R. McClean, T. McCourt, M. McEwen, A. Megrant, B. Meurer Costa, X. Mi, K. C. Miao, M. Mohseni, S. Montazeri, A. Morvan, E. Mount, W. Mruczkiewicz, O. Naaman, M. Neeley, C. Neill, A. Nersisyan, H. Neven, M. Newman, J. H. Ng, A. Nguyen, M. Nguyen, M. Y. Niu, T. E. O'Brien, A. Opremcak, J. Platt, A. Petukhov, R. Potter, L. P. Pryadko, C. Quintana, P. Roushan, N. C. Rubin, N. Saei, D. Sank, K. Sankaragomathi, K. J. Satzinger, H. F. Schurkus, C. Schuster, M. J. Shearn, A. Shorter, V. Shvarts, J. Skruzny, V. Smelyanskiy, W. C. Smith, G. Sterling, D. Strain, M. Szalay, A. Torres, G. Vidal, B. Villalonga, C. Vollgraff Heidweiller, T. White, C. Xing, Z. J. Yao, P. Yeh, J. Yoo, G. Young, A. Zalcman, Y. Zhang, N. Zhu, and G. Q. AI, Suppressing quantum errors by scaling a surface code logical qubit, *Nature* **614**, 676 (2023).
- [10] R. Acharya, D. A. Abanin, L. Aghababaie-Beni, I. Aleiner, T. I. Andersen, M. Ansmann, F. Arute, K. Arya, A. Asfaw, N. Astrakhantsev, J. Atalaya, R. Babbush, D. Bacon, B. Ballard, J. C. Bardin, J. Bausch, A. Bengtsson, A. Bilmes, S. Blackwell, S. Boixo, G. Bortoli, A. Bourassa, J. Bovaird, L. Brill, M. Broughton, D. A. Browne, B. Buchea, B. B. Buckley, D. A. Buell, T. Burger, B. Burkett, N. Bushnell, A. Cabrera, J. Campero, H.-S. Chang, Y. Chen, Z. Chen, B. Chiaro, D. Chik, C. Chou, J. Claes, A. Y. Cleland, J. Cogan, R. Collins, P. Conner, W. Courtney, A. L. Crook, B. Curtin, S. Das, A. Davies, L. De Lorenzo, D. M. Debroy, S. Demura, M. Devoret, A. Di Paolo, P. Donohoe, I. Drozdov, A. Dunsworth, C. Earle, T. Edlich, A. Eickbusch, A. M. Elbag, M. Elzouka, C. Erickson, L. Faoro, E. Farhi, V. S. Ferreira, L. F. Burgos, E. Forati, A. G. Fowler, B. Foxen, S. Ganjam, G. Garcia, R. Gasca, É. Genois, W. Giang, C. Gidney, D. Gilboa, R. Gosula, A. G. Dau, D. Graumann, A. Greene, J. A. Gross, S. Habegger, J. Hall, M. C. Hamilton, M. Hansen, M. P. Harrigan, S. D. Harrington, F. J. H. Heras, S. Heslin, P. Heu, O. Higgott, G. Hill, J. Hilton, G. Holland, S. Hong, H.-Y. Huang, A. Huff, W. J. Huggins, L. B. Ioffe, S. V. Isakov, J. Iveland, E. Jeffrey, Z. Jiang, C. Jones, S. Jordan, C. Joshi, P. Juhas, D. Kafri, H. Kang, A. H. Karamlou, K. Kechedzhi, J. Kelly, T. Khairé, T. Khatarr, M. Khezri, S. Kim, P. V. Klimov, A. R. Klots, B. Kobrin, P. Kohli, A. N. Korotkov, F. Kostritsa, R. Kothari, B. Kozlovskii, J. M. Kreikebaum, V. D. Kurilovich, N. Lacroix, D. Landhuis, T. Lange-Dei, B. W. Langle, P. Laptev, K.-M. Lau, L. Le Guevel, J. Ledford, J. Lee, K. Lee, Y. D. Lensky, S. Leon, B. J. Lester, W. Y. Li, Y. Li, A. T. Lill, W. Liu, W. P. Livingston, A. Locharla, E. Lucero, D. Lundahl, A. Lunt, S. Madhuk, F. D. Malone, A. Maloney, S. Mandrà, J. Manyika, L. S. Martin, O. Martin, S. Martin, C. Maxfield, J. R. McClean, M. McEwen, S. Meeks, A. Megrant, X. Mi, K. C. Miao, A. Mieszala, R. Molavi, S. Molina, S. Montazeri, A. Morvan, R. Movassagh, W. Mruczkiewicz, O. Naaman, M. Neeley, C. Neill, A. Nersisyan, H. Neven, M. Newman, J. H. Ng, A. Nguyen, M. Nguyen, C.-H. Ni, M. Y. Niu, T. E. O'Brien, W. D. Oliver, A. Opremcak, K. Ottosson, A. Petukhov, A. Pizzuto, J. Platt, R. Potter, O. Pritchard, L. P. Pryadko, C. Quintana, G. Ramachandran, M. J. Reagor, J. Redding, D. M. Rhodes, G. Roberts, E. Rosenberg, E. Rosenfeld, P. Roushan, N. C. Rubin, N. Saei, D. Sank, K. Sankaragomathi, K. J. Satzinger, H. F. Schurkus, C. Schuster, A. W. Senior, M. J. Shearn, A. Shorter, N. Shutty, V. Shvarts, S. Singh, V. Sivak, J. Skruzny, S. Small, V. Smelyanskiy, W. C. Smith, R. D. Somma, S. Springer, G. Sterling, D. Strain, J. Suchard, A. Szasz, A. Szein, D. Thor, A. Torres, M. M. Torunbalci, A. Vaishnav, J. Vargas, S. Vdovichev, G. Vidal, B. Villalonga, C. V. Heidweiller, S. Waltman, S. X. Wang, B. Ware, K. Weber, T. Weidel, T. White, K. Wong, B. W. K. Woo, C. Xing, Z. J. Yao, P. Yeh, B. Ying, J. Yoo, N. Yosri, G. Young, A. Zalcman, Y. Zhang, N. Zhu, N. Zobrist, G. Q. AI, and Collaborators, Quantum error correction below the surface code threshold, *Nature* (2024).
- [11] N. Lacroix, A. Bourassa, F. J. H. Heras, L. M. Zhang, J. Bausch, A. W. Senior, T. Edlich, N. Shutty, V. Sivak, A. Bengtsson, M. McEwen, O. Higgott, D. Kafri, J. Claes, A. Morvan, Z. Chen, A. Zalcman, S. Madhuk, R. Acharya, L. Aghababaie Beni, G. Aigeldinger, R. Alcaraz, T. I. Andersen, M. Ansmann, F. Arute, K. Arya, A. Asfaw, J. Atalaya, R. Babbush, B. Ballard, J. C. Bardin, A. Bilmes, S. Blackwell, J. Bovaird, D. Bowers, L. Brill, M. Broughton, D. A. Browne, B. Buchea, B. B. Buckley, T. Burger, B. Burkett, N. Bushnell, A. Cabrera, J. Campero, H.-S. Chang, B. Chiaro, L.-Y. Chih, A. Y. Cleland, J. Cogan, R. Collins, P. Conner, W. Courtney, A. L. Crook, B. Curtin, S. Das, S. Demura, L. De Lorenzo, A. Di Paolo, P. Donohoe, I. Drozdov, A. Dunsworth, A. Eickbusch, A. M. Elbag, M. Elzouka, C. Erickson, V. S. Ferreira, L. Flores Burgos, E. Forati, A. G. Fowler, B. Foxen, S. Ganjam, G. Garcia, R. Gasca, É. Genois, W. Giang, D. Gilboa, R. Gosula, A. Grajales Dau, D. Graumann, A. Greene, J. A. Gross, T. Ha, S. Habegger, M. Hansen, M. P. Harrigan, S. D. Harrington, S. Heslin, P. Heu, R. Hiltermann, J. Hilton, S. Hong, H.-Y. Huang, A. Huff, W. J. Huggins, E. Jeffrey, Z. Jiang, X. Jin, C. Joshi, P. Juhas, A. Kabel, H. Kang, A. H. Karamlou, K. Kechedzhi, T. Khairé, T. Khatarr, M. Khezri, S. Kim, P. V. Klimov, B. Kobrin, A. N. Korotkov, F. Kostritsa, J. M. Kreikebaum, V. D. Kurilovich, D. Landhuis, T. Lange-Dei, B. W. Langle, P. Laptev, K.-M. Lau, J. Ledford, K. Lee, B. J. Lester, L. Le Guevel, W. Y. Li, Y. Li, A. T. Lill, W. P. Livingston, A. Locharla, E. Lucero, D. Lundahl, A. Lunt, A. Maloney, S. Mandrà, L. S. Martin, O. Martin, C. Maxfield, J. R. McClean, S. Meeks, A. Megrant, K. C. Miao, R. Molavi, S. Molina, S. Montazeri, R. Movassagh, C. Neill, M. Newman, A. Nguyen, M. Nguyen, C.-H. Ni, M. Y. Niu, L. Oas, W. D. Oliver, R. Orosco, K. Ottosson, A. Pizzuto, R. Potter, O. Pritchard, C. Quintana, G. Ramachandran, M. J. Reagor, R. Resnick, D. M. Rhodes, G. Roberts, E. Rosenberg, E. Rosenfeld, E. Rossi, P. Roushan, K. Sankaragomathi, H. F. Schurkus, M. J. Shearn, A. Shorter, V. Shvarts, S. Small, W. C. Smith, S. Springer, G. Sterling, J. Suchard, A. Szasz, A. Szein, D. Thor, E. Tomita, A. Torres, M. M. Torunbalci, A. Vaishnav, J. Vargas, S. Vdovichev, G. Vidal, C. Vollgraff Heidweiller, S. Waltman, J. Waltz, S. X. Wang, B. Ware, T. Weidel, T. White, K. Wong, B. W. K. Woo, M. Woodson, C. Xing, Z. J. Yao, P. Yeh, B. Ying, J. Yoo, N. Yosri, G. Young, Y. Zhang, N. Zhu, N. Zobrist, H. Neven, P. Kohli, A. Davies, S. Boixo, J. Kelly, C. Jones, C. Gidney, and K. J. Satzinger, Scaling and logic in the color code on a superconducting quantum

- processor, *Nature* (2025).
- [12] L. Egan, D. M. Debroy, C. Noel, A. Risinger, D. Zhu, D. Biswas, M. Newman, M. Li, K. R. Brown, M. Cetina, *et al.*, Fault-tolerant control of an error-corrected qubit, *Nature* **598**, 281 (2021).
 - [13] C. Ryan-Anderson, J. G. Bohnet, K. Lee, D. Gresh, A. Hankin, J. Gaebler, D. Francois, A. Chernoguzov, D. Lucchetti, N. C. Brown, *et al.*, Realization of real-time fault-tolerant quantum error correction, *Phys. Rev. X* **11**, 041058 (2021).
 - [14] J. Hilder, D. Pijn, O. Onishchenko, A. Stahl, M. Orth, B. Lekitsch, A. Rodriguez-Blanco, M. Müller, F. Schmidt-Kaler, and U. G. Poschinger, Fault-tolerant parity read-out on a shuttling-based trapped-ion quantum computer, *Phys. Rev. X* **12**, 011032 (2022).
 - [15] D. Bluvstein, H. Levine, G. Semeghini, T. T. Wang, S. Ebadi, M. Kalinowski, A. Keesling, N. Maskara, H. Pichler, M. Greiner, *et al.*, A quantum processor based on coherent transport of entangled atom arrays, *Nature* **604**, 451 (2022).
 - [16] S. Ebadi, T. T. Wang, H. Levine, A. Keesling, G. Semeghini, A. Omran, D. Bluvstein, R. Samajdar, H. Pichler, W. W. Ho, *et al.*, Quantum phases of matter on a 256-atom programmable quantum simulator, *Nature* **595**, 227 (2021).
 - [17] P. S. Rodriguez, J. M. Robinson, P. N. Jepsen, Z. He, C. Duckering, C. Zhao, K.-H. Wu, J. Campo, K. Bagnall, M. Kwon, T. Karolyshyn, P. Weinberg, M. Cain, S. J. Evered, A. A. Geim, M. Kalinowski, S. H. Li, T. Manovitz, J. Amato-Grill, J. I. Basham, L. Bernstein, B. Braverman, A. Bylinskii, A. Choukri, R. DeAngelo, F. Fang, C. Fieweger, P. Frederick, D. Haines, M. Hamdan, J. Hammett, N. Hsu, M.-G. Hu, F. Huber, N. Jia, D. Kedar, M. Kornjača, F. Liu, J. Long, J. Lopatin, P. L. S. Lopes, X.-Z. Luo, T. Macrì, O. Marković, L. A. Martínez-Martínez, X. Meng, S. Ostermann, E. Ostroumov, D. Paquette, Z. Qiang, V. Shofman, A. Singh, M. Singh, N. Sinha, H. Thoreen, N. Wan, Y. Wang, D. Waxman-Lenz, T. Wong, J. Wurtz, A. Zhdanov, L. Zheng, M. Greiner, A. Keesling, N. Gemelke, V. Vuletić, T. Kitagawa, S.-T. Wang, D. Bluvstein, M. D. Lukin, A. Lukin, H. Zhou, and S. H. Cantú, Experimental demonstration of logical magic state distillation, *Nature* (2025).
 - [18] D. Bluvstein, A. A. Geim, S. H. Li, S. J. Evered, J. P. B. Ataiades, G. Baranes, A. Gu, T. Manovitz, M. Xu, M. Kalinowski, S. Majidy, C. Kokail, N. Maskara, E. C. Trapp, L. M. Stewart, S. Hollerith, H. Zhou, M. J. Gullans, S. F. Yelin, M. Greiner, V. Vuletic, M. Cain, and M. D. Lukin, Architectural mechanisms of a universal fault-tolerant quantum computer, *arXiv preprint arXiv:2506.20661* (2025).
 - [19] A. Y. Kitaev, Fault-tolerant quantum computation by anyons, *Annals of Physics* **303**, 2 (2003).
 - [20] S. B. Bravyi and A. Y. Kitaev, Quantum codes on a lattice with boundary, *arXiv preprint quant-ph/9811052* (1998).
 - [21] E. Dennis, A. Kitaev, A. Landahl, and J. Preskill, Topological quantum memory, *Journal of Mathematical Physics* **43**, 4452 (2002).
 - [22] A. G. Fowler, M. Mariantoni, J. M. Martinis, and A. N. Cleland, Surface codes: Towards practical large-scale quantum computation, *Phys. Rev. A* **86**, 032324 (2012).
 - [23] B. M. Terhal, Quantum error correction for quantum memories, *Rev. Mod. Phys.* **87**, 307 (2015).
 - [24] L. Skoric, D. E. Browne, K. M. Barnes, N. I. Gillespie, and E. T. Campbell, Parallel window decoding enables scalable fault tolerant quantum computation, *Nature Communications* **14**, 7040 (2023).
 - [25] X. Tan, F. Zhang, R. Chao, Y. Shi, and J. Chen, Scalable surface-code decoders with parallelization in time, *PRX Quantum* **4**, 040344 (2023).
 - [26] L. Caune, L. Skoric, N. S. Blunt, A. Ruban, J. McDaniel, J. A. Valery, A. D. Patterson, A. V. Gramolin, J. Majaniemi, K. M. Barnes, *et al.*, Demonstrating real-time and low-latency quantum error correction with superconducting qubits, *arXiv preprint arXiv:2410.05202* (2024).
 - [27] D. S. Wang, A. G. Fowler, and L. C. Hollenberg, Surface code quantum computing with error rates over 1%, *Phys. Rev. A* **83**, 020302 (2011).
 - [28] A. G. Fowler, Minimum weight perfect matching of fault-tolerant topological quantum error correction in average $o(1)$ parallel time, *arXiv preprint arXiv:1307.1740* (2013).
 - [29] Y. Wu and L. Zhong, Fusion blossom: Fast mwpm decoders for qec, in *2023 IEEE International Conference on Quantum Computing and Engineering (QCE)*, Vol. 1 (IEEE, 2023) pp. 928–938.
 - [30] O. Higgott and C. Gidney, Sparse blossom: correcting a million errors per core second with minimum-weight matching, *Quantum* **9**, 1600 (2025).
 - [31] N. Delfosse and N. H. Nickerson, Almost-linear time decoding algorithm for topological codes, *Quantum* **5**, 595 (2021).
 - [32] S. Huang, M. Newman, and K. R. Brown, Fault-tolerant weighted union-find decoding on the toric code, *Phys. Rev. A* **102**, 012419 (2020).
 - [33] G. Duclos-Cianci and D. Poulin, Fast decoders for topological quantum codes, *Phys. Rev. Lett.* **104**, 050504 (2010).
 - [34] G. Duclos-Cianci and D. Poulin, Fast decoders for topological quantum codes, *Phys. Rev. Lett.* **104**, 050504 (2010).
 - [35] K.-Y. Kuo and C.-Y. Lai, Generalized quantum data-syndrome codes and belief propagation decoding for phenomenological noise, *IEEE Tran. Inf. Theory*, 1 (2025).
 - [36] K.-Y. Kuo and C.-Y. Lai, Fault-tolerant belief propagation for practical quantum memory, *arXiv preprint arXiv:2409.18689* (2024).
 - [37] A. Hutter, J. R. Wootton, and D. Loss, Efficient markov chain monte carlo algorithm for the surface code, *Phys. Review A* **89**, 022326 (2014).
 - [38] A. S. Darmawan and D. Poulin, Tensor-network simulations of the surface code under realistic noise, *Phys. Rev. Lett.* **119**, 040502 (2017).
 - [39] A. S. Darmawan and D. Poulin, Linear-time general decoding algorithm for the surface code, *Phys. Rev. E* **97**, 051302 (2018).
 - [40] S. Varsamopoulos, B. Criger, and K. Bertels, Decoding small surface codes with feedforward neural networks, *Quantum Science and Technology* **3**, 015004 (2017).
 - [41] X. Ni, Neural network decoders for large-distance 2d toric codes, *Quantum* **4**, 310 (2020).
 - [42] C. Chamberland and P. Ronagh, Deep neural decoders for near term fault-tolerant experiments, *Quantum Science and Technology* **3**, 044002 (2018).
 - [43] R. Sweke, M. S. Kesselring, E. P. van Nieuwenburg, and J. Eisert, Reinforcement learning decoders for fault-tolerant quantum computation, *Machine Learning: Science and Technology* **2**, 025005 (2020).

- [44] M. Zhang, X. Ren, G. Xi, Z. Zhang, Q. Yu, F. Liu, H. Zhang, S. Zhang, and Y.-C. Zheng, A scalable, fast and programmable neural decoder for fault-tolerant quantum computation using surface codes, arXiv preprint arXiv:2305.15767 (2023).
- [45] C. Chamberland, L. Goncalves, P. Sivarajah, E. Peterson, and S. Grimberg, Techniques for combining fast local decoders with global decoders under circuit-level noise, *Quantum Science and Technology* **8**, 045011 (2023).
- [46] J. Bausch, A. W. Senior, F. J. Heras, T. Edlich, A. Davies, M. Newman, C. Jones, K. Satzinger, M. Y. Niu, S. Blackwell, G. Holland, D. Kafri, J. Atalaya, C. Gidney, D. Hassabis, S. Boixo, H. Neven, and P. Kohli, Learning high-accuracy error decoding for quantum processors, *Nature* **635**, 834 (2024).
- [47] A. deMarti iOlius, P. Fuentes, R. Orús, P. M. Crespo, and J. E. Martinez, Decoding algorithms for surface codes, *Quantum* **8**, 1498 (2024).
- [48] P. Das, C. A. Pattison, S. Manne, D. M. Carmean, K. M. Svore, M. Qureshi, and N. Delfosse, Afs: Accurate, fast, and scalable error-decoding for fault-tolerant quantum computers, in *2022 IEEE International Symposium on High-Performance Computer Architecture (HPCA)* (IEEE, 2022) pp. 259–273.
- [49] N. Liyanage, Y. Wu, A. Deters, and L. Zhong, Scalable quantum error correction for surface codes using fpga, in *2023 IEEE International Conference on Quantum Computing and Engineering (QCE)*, Vol. 1 (IEEE, 2023) pp. 916–927.
- [50] B. Barber, K. M. Barnes, T. Bialas, O. Buğdaycı, E. T. Campbell, N. I. Gillespie, K. Johar, R. Rajan, A. W. Richardson, L. Skoric, C. Topal, M. L. Turner, and A. B. Ziad, A real-time, scalable, fast and resource-efficient decoder for a quantum computer, *Nature Electronics* **8**, 84 (2025).
- [51] Y. Wu, N. Liyanage, and L. Zhong, Micro blossom: Accelerated minimum-weight perfect matching decoding for quantum error correction, in *Proceedings of the 30th ACM International Conference on Architectural Support for Programming Languages and Operating Systems (ASPLOS), Volume 2* (ACM, 2025) p. 639–654.
- [52] A. G. Fowler, Optimal complexity correction of correlated errors in the surface code, arXiv preprint arXiv:1310.0863 (2013).
- [53] N. Delfosse and J.-P. Tillich, A decoding algorithm for CSS codes using the X/Z correlations, in *2014 IEEE International Symposium on Information Theory* (2014) pp. 1071–1075.
- [54] Y. Yuan and C.-C. Lu, A modified mwpm decoding algorithm for quantum surface codes over depolarizing channels, in *2022 International Symposium on Information Theory and Its Applications (ISITA)* (IEEE, 2022) pp. 204–208.
- [55] A. d. iOlius, J. E. Martinez, P. Fuentes, and P. M. Crespo, Performance enhancement of surface codes via recursive minimum-weight perfect-match decoding, *Phys. Rev. A* **108**, 022401 (2023).
- [56] T.-H. Lin and C.-Y. Lai, Union-intersection union-find for decoding depolarizing errors in topological codes, *IEEE Journal on Selected Areas in Information Theory* (2025).
- [57] IRMWPM: Iterative Reweighting Minimum-Weight Perfect Matching, <https://github.com/kampfen-hub/FTIR> (2025), accessed on 8 September 2025.
- [58] A. G. Fowler, A. C. Whiteside, A. L. McInnes, and A. Rabhani, Topological code autotune, *Phys. Rev. X* **2**, 041003 (2012).
- [59] A. Paler and A. G. Fowler, Pipelined correlated minimum weight perfect matching of the surface code, *Quantum* **7**, 1205 (2023).